



# CeO<sub>2</sub> morphology-dependent NbO<sub>x</sub>–CeO<sub>2</sub> interaction, structure and catalytic performance of NbO<sub>x</sub>/CeO<sub>2</sub> catalysts in oxidative dehydrogenation of propane



Yiming Liu, Liangfeng Luo, Yuxian Gao, Weixin Huang\*

Hefei National Laboratory for Physical Sciences at the Microscale, CAS Key Laboratory of Materials for Energy Conversion and Department of Chemical Physics, University of Science and Technology of China, Hefei 230026, China

## ARTICLE INFO

### Article history:

Received 30 November 2015

Received in revised form 2 February 2016

Accepted 5 March 2016

Available online 8 March 2016

### Keywords:

Metal-support interaction

CeO<sub>2</sub> nanocrystals

Nb<sub>2</sub>O<sub>5</sub>

CeNbO<sub>4</sub>

Oxygen vacancy

## ABSTRACT

A series of NbO<sub>x</sub>/CeO<sub>2</sub> catalysts were synthesized employing CeO<sub>2</sub> cubes (c-CeO<sub>2</sub>), CeO<sub>2</sub> rods calcined at 500 °C (r-CeO<sub>2</sub>-500) and CeO<sub>2</sub> rods calcined at 700 °C (r-CeO<sub>2</sub>-700) as the supports, and their structures and catalytic performances in the oxidative dehydrogenation of propane reaction were studied. Strong CeO<sub>2</sub> morphology-dependent NbO<sub>x</sub>–CeO<sub>2</sub> interaction, structure and catalytic performance of NbO<sub>x</sub>/CeO<sub>2</sub> catalysts were observed. The supported NbO<sub>x</sub> species evolve with the increasing Nb loading from the monomeric Nb species to the polymeric Nb species and the CeNbO<sub>4</sub> species. The monomeric Nb<sup>5+</sup> species interacting with oxygen vacancy/Ce<sup>3+</sup> on CeO<sub>2</sub> can be reduced to form the monomeric Nb<sup>4+</sup> species. The formed monomeric Nb species follows the order of NbO<sub>x</sub>/r-CeO<sub>2</sub>-500 > NbO<sub>x</sub>/c-CeO<sub>2</sub> > NbO<sub>x</sub>/r-CeO<sub>2</sub>-700 while the formed monomeric Nb<sup>4+</sup> species is most abundant on the c-CeO<sub>2</sub> support. The loading of NbO<sub>x</sub> suppresses the surface reduction of c-CeO<sub>2</sub> and r-CeO<sub>2</sub>-500 but promotes the surface reduction of r-CeO<sub>2</sub>-700. R-CeO<sub>2</sub>-500 and r-CeO<sub>2</sub>-700 are more catalytic active than c-CeO<sub>2</sub> in the oxidative dehydrogenation of propane reaction. The loading of NbO<sub>x</sub> slightly enhances the catalytic activity of c-CeO<sub>2</sub> but decreases the catalytic activity of r-CeO<sub>2</sub>-700. A loading of 0.6 Nb/nm<sup>2</sup> much enhances the catalytic activity of r-CeO<sub>2</sub>-500 at 200 °C, but further increasing the Nb loading results in the decrease of the C<sub>3</sub>H<sub>8</sub> conversion. These results add a solid example to vindicate the morphology engineering strategy to modify the structure and catalytic performance of CeO<sub>2</sub>-based catalysts.

© 2016 Elsevier B.V. All rights reserved.

## 1. Introduction

Oxidative dehydrogenation of alkanes to corresponding alkenes represents an economic and environmental-friendly process to produce alkenes [1–4]. Propene, an important raw material in the modern chemical industry, is mainly produced by steam cracking, fluid-catalytic-cracking (FCC), and catalytic propane dehydrogenation [5], but these processes suffer from thermodynamics limit, high reaction temperature and rapid coking of catalysts. Oxidative dehydrogenation of propane (ODHP) has been recently explored as an alternative process to produce propene [6–10]. The ODHP reaction is strongly exothermic and can proceed below 500 °C; meanwhile, the presence of O<sub>2</sub> in the ODHP reaction significantly alleviates the coking of catalysts. However, it remains as a great challenge for the ODHP reaction to seek a suitable catalyst to

achieve a high propene selectivity in the presence of oxygen with high conversions of propane.

The ODHP reaction catalyzed by transitional metal oxides generally follows the Mars van Krevelen mechanism [11], in which the oxidation of propane by surface lattice oxygen of transitional metal oxides is the rate-limiting step. Due to its nice Redox property and high oxygen storage capacity, CeO<sub>2</sub> has been widely used in the catalysts for the ODHP reaction [12–17]. NbO<sub>x</sub> has also been demonstrated as a component of active mixed oxides for oxidative dehydrogenation reactions [18–25]. Although reported to be active for several reactions [26–30], NbO<sub>x</sub>–CeO<sub>2</sub>-based catalysts have been seldom reported as catalysts for the ODHP reaction except a report on the low-temperature catalytic performance of nanosized CeNbNiO mixed oxides for the ODHP reaction by Li et al. [31].

Interactions among different components of mixed oxides strongly affect their structure and catalytic performance. Recent progresses in catalysis of CeO<sub>2</sub> nanocrystals demonstrate the CeO<sub>2</sub> morphology as a new and effective macroscopic structural parameter to modify the surface chemistry and catalysis of

\* Corresponding author.

E-mail address: [huangwx@ustc.edu.cn](mailto:huangwx@ustc.edu.cn) (W. Huang).

CeO<sub>2</sub> [32–36]. Wu et al. observed CeO<sub>2</sub> morphology-dependent VO<sub>x</sub>–CeO<sub>2</sub> interactions and VO<sub>x</sub> species in VO<sub>x</sub>/CeO<sub>2</sub> catalysts [37–39] and correlated their catalytic activity in the oxidative dehydrogenation of isobutene to the oxygen vacancy concentration of CeO<sub>2</sub> support [37]. In this paper we explored CeO<sub>2</sub>-supported NbO<sub>x</sub> catalysts for the ODHP reaction. Various CeO<sub>2</sub> nanocrystals with different morphologies were used as the supports and CeO<sub>2</sub> morphology-dependent NbO<sub>x</sub>–CeO<sub>2</sub> interaction, structure and catalytic performance of NbO<sub>x</sub>/CeO<sub>2</sub> were observed.

## 2. Experimental

### 2.1. Catalyst preparation

All chemical reagents with the A.R. grade were purchased from Sinopharm Chemical Reagent Co., Ltd. and used as received. The synthesis of cubes (denoted as c-CeO<sub>2</sub>) and CeO<sub>2</sub> rod precursor followed the Mai et al.'s recipe [32]. Typically, 1.96 g Ce(NO<sub>3</sub>)<sub>3</sub>·6H<sub>2</sub>O was dissolved in 40 mL ultrapure water (resistance >18 MΩ) and 16.88 g NaOH was dissolved in 30 mL ultrapure water. The NaOH solution was added dropwise into the Ce(NO<sub>3</sub>)<sub>3</sub> solution under stirring at RT. The mixed solution was adequately stirred for additional 30 min at room temperature and then transferred into a 100-mL Teflon bottle. The Teflon bottle was tightly sealed and hydrothermally treated in a stainless-steel autoclave. To prepare CeO<sub>2</sub> cubes, the hydrothermal treatment proceeded at 180 °C for 24 h. After cooling, the obtained precipitate was collected, washed with ultrapure water, and dried in vacuo at 80 °C for 16 h. Then the acquired powder was calcined in muffle oven at 500 °C for 4 h to acquire CeO<sub>2</sub> cubes. To prepare CeO<sub>2</sub> rods, the hydrothermal treatment proceeded at 100 °C for 24 h. After cooling, the obtained precipitate was collected, washed with ultrapure water, and dried in vacuo at 80 °C for 16 h. Then the acquired CeO<sub>2</sub> rod precursor was calcined in muffle oven at 500 and 700 °C for 4 h to acquire two types of CeO<sub>2</sub> rods, respectively denoted as r-CeO<sub>2</sub>-500 and r-CeO<sub>2</sub>-700.

NbO<sub>x</sub>/CeO<sub>2</sub> catalysts were prepared by conventional wetness incipient impregnation method. Typically, the calculated amount of niobium (V) oxalate hydrate (Nb(HC<sub>2</sub>O<sub>4</sub>)<sub>5</sub>·nH<sub>2</sub>O, molecular weight of 538.04 after dehydration) was dissolved in 0.5 mL ultrapure water at 50 °C and 0.5 g CeO<sub>2</sub> nanocrystals were added to the acquired aqueous solution. The mixture was ultra-sonicated at 50 °C for 30 min and then dried at 110 °C for 12 h. The acquired catalyst precursor was calcined under ambient atmosphere at 400 °C for 4 h to prepare the NbO<sub>x</sub>/CeO<sub>2</sub> catalyst.

### 2.2. Catalyst characterizations

Compositions of catalysts were analyzed with a Perkin Elmer Optima 7300 DV inductively coupled plasma-atomic emission spectrometer (ICP-AES). TG-DTA analysis was performed in air on a TA SDT Q600 thermal gravimetric analyzer with a heat rate of 10 °C/min. BET specific surface areas were acquired on a Micromeritics Tristar II 3020M surface area analyzer. Catalysts were degassed at 300 °C prior to the measurements. Powder X-ray diffraction (XRD) patterns were recorded on a Philips X'Pert Pro Super diffractometer with Cu Kα radiation (λ = 0.15406 nm) operating at 40 kV and 50 mA. Transmission electron microscopy (TEM) and high-resolution transmission electron microscopy (HRTEM) images were performed by using JEOL-2010 and JEOL-2100F high-resolution transmission electron microscopes with the electron acceleration energy of 200 kV. Laser Raman spectra were obtained by using a Renishaw inVia confocal Raman microscope spectrograph with the excitation line at 532 nm at ambient conditions. X-ray photoelectron spectra were acquired on an ESCALAB 250 high-performance electron spectrometer using monochromatized

AlKα (hν = 1486.7 eV) as the excitation source. The likely charging of samples was corrected by setting the binding energy of the adventitious carbon (C1s) to 284.8 eV. H<sub>2</sub>-temperature-programmed reduction (H<sub>2</sub>-TPR) experiments were performed on a home-established apparatus equipped with a thermal conductivity detector (TCD) to detect the H<sub>2</sub> consumption. 50 mg catalysts was placed in a quartz reactor and heated in a flow of 5% H<sub>2</sub>/Ar mixture (flow rate: 30 mL/min) up to 700 °C at a heating rate of 10 °C/min.

### 2.3. Catalytic performance evaluation

The catalytic activity of the NbO<sub>x</sub>/CeO<sub>2</sub> catalysts in the ODHP reaction were evaluated with a fixed-bed flow reactor. 100 mg catalyst (60–80 mesh) was placed in a quartz reactor and the reaction gas consisting of C<sub>3</sub>H<sub>8</sub>, O<sub>2</sub> and Ar (C<sub>3</sub>H<sub>8</sub>:O<sub>2</sub>:Ar = 1.2:1.0:1.2) was fed at a GHSV of 10,000 mL h<sup>−1</sup> g<sup>−1</sup>. The catalyst was heated to the desired reaction temperatures at a rate of 2 °C/min. In our experimental setup the thermocouple was fixed to the outer surface of the quartz reactor corresponding to the catalyst bed. The reported temperatures were expected to be lower than the actual temperatures of the catalyst bed at larger propane conversions because of the strongly exothermic ODHP reaction. After the reaction reached the steady state, the composition of effluent gas was analyzed with two online Fuli 9750 gas chromatographs. One was equipped with TDX-01 carbon-zeolite column and TCD detector for the separation and detection of O<sub>2</sub>, CO and CO<sub>2</sub>; the other with RESTEK Rt-Alumina BOND/Na<sub>2</sub>SO<sub>4</sub> capillary column and H<sub>2</sub>-flame ionization detector for the separation and detection of hydrocarbons. The propane conversion and propene selectivity were calculated as the following:

$$\text{C}_3\text{H}_8\text{conversion} = ([\text{C}_3\text{H}_8]_{\text{inlet}} - [\text{C}_3\text{H}_8]_{\text{outlet}}) / [\text{C}_3\text{H}_8]_{\text{inlet}} \times 100\%$$

$$\text{C}_3\text{H}_6\text{selectivity} = [\text{C}_3\text{H}_6]_{\text{outlet}} / ([\text{C}_3\text{H}_8]_{\text{inlet}} - [\text{C}_3\text{H}_8]_{\text{outlet}}) \times 100\%$$

## 3. Results and discussion

Fig. 1A–C shows typical TEM and HRTEM images of c-CeO<sub>2</sub>, r-CeO<sub>2</sub>-500 and r-CeO<sub>2</sub>-700 nanocrystals. CeO<sub>2</sub> nanocrystals in c-CeO<sub>2</sub> exhibit a uniform cubic morphology with the edge lengths of 10–30 nm. CeO<sub>2</sub> nanocrystals in r-CeO<sub>2</sub>-500 exhibit rod morphologies with the diameter of ~5 nm and the lengths of 20–200 nm. CeO<sub>2</sub> nanocrystals in r-CeO<sub>2</sub>-700 exhibit both rod morphologies with the diameter of ~5 nm and the lengths of 10–100 nm and irregular aggregates larger than 20 nm. This demonstrates that the morphology of CeO<sub>2</sub> nanocrystals prepared by the calcination of CeO<sub>2</sub> rod precursors depends on the calcination temperature. Agreeing with previous reports [32,34,40], lattice fringes of CeO<sub>2</sub>{100} facets dominate in the HRTEM images of c-CeO<sub>2</sub>, lattice fringes of CeO<sub>2</sub>{110} and {100} facets dominate in the HRTEM images of r-CeO<sub>2</sub>-500 and lattice fringes of CeO<sub>2</sub>{111} facets dominate in the HRTEM images of r-CeO<sub>2</sub>-700. There is no doubt that c-CeO<sub>2</sub> is enclosed with six {100} facets and r-CeO<sub>2</sub>-500 is more defective than c-CeO<sub>2</sub> and r-CeO<sub>2</sub>-700; however, uncertainty exist on the facets exposed on CeO<sub>2</sub> rods [34,41]. On the basis of our works on CeO<sub>2</sub> nanocrystals [33–36], we propose that r-CeO<sub>2</sub>-500 exposes mainly CeO<sub>2</sub>{110} and {100} facets while r-CeO<sub>2</sub>-700 exposes mainly CeO<sub>2</sub>{111} and {110} facets.

Prior to the preparation of NbO<sub>x</sub>/CeO<sub>2</sub> catalysts, we studied the decomposition behaviors of Nb(HC<sub>2</sub>O<sub>4</sub>)<sub>5</sub>·nH<sub>2</sub>O in air by TGA analysis (Fig. 2A). An obvious weight loss up to 135 °C corresponded to the dehydration process of Nb(HC<sub>2</sub>O<sub>4</sub>)<sub>5</sub>·nH<sub>2</sub>O and the subsequent intense weight loss up to 330 °C corresponded to the decomposition process of Nb(HC<sub>2</sub>O<sub>4</sub>)<sub>5</sub>. No weight loss was observed until



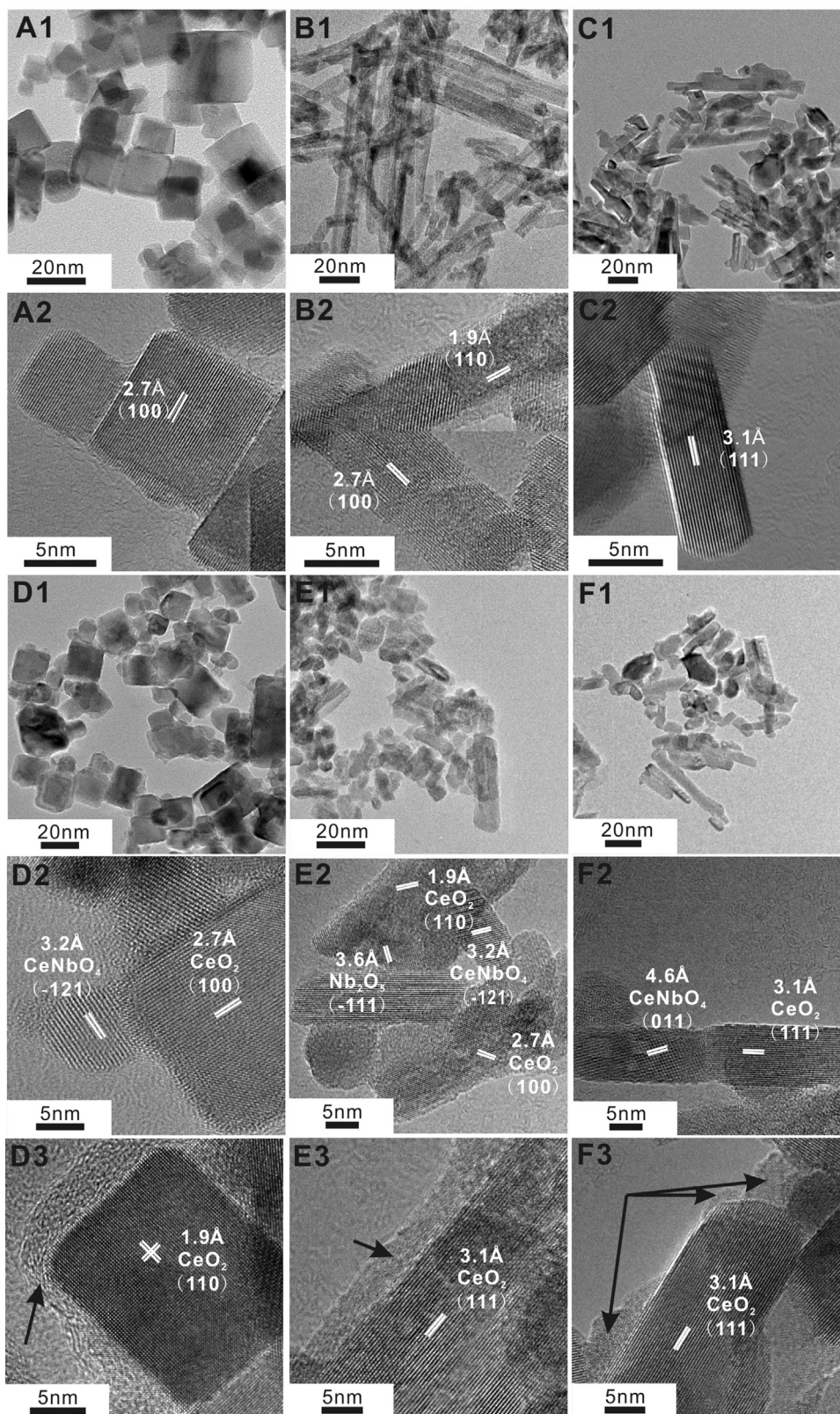


**Fig. 1.** Representative TEM and HRTEM images of (A1 and A2) c-CeO<sub>2</sub>, (B1 and B2) r-CeO<sub>2</sub>-500, (C1 and C2) r-CeO<sub>2</sub>-700, (D1–D3) 8.7Nb/r-CeO<sub>2</sub>, (E1–E3) 9.9Nb/r-CeO<sub>2</sub>-500 and (F1–F3) 10.2Nb/r-CeO<sub>2</sub>-700. The areas indicated by the arrows in Fig. D3, E3 and F3 correspond to observed amorphous structures.

a weak weight loss occurred between 535 and 645 °C. We thus chose 400 °C as the calcination temperature for the preparation of NbO<sub>x</sub>/CeO<sub>2</sub> catalysts. However, the sample prepared by calcining Nb(HC<sub>2</sub>O<sub>4</sub>)<sub>5</sub>·nH<sub>2</sub>O in air at 400 °C for 4 h did not show any XRD

patterns (Fig. 2B), indicating that it should be amorphous niobium oxides (denoted as NbO<sub>x</sub>).

The compositions of various NbO<sub>x</sub>/CeO<sub>2</sub> catalysts were determined by ICP-AES and the BET specific surface areas of c-CeO<sub>2</sub>,

**Table 1**

BET surface areas of CeO<sub>2</sub> nanocrystals and catalytic performances of CeO<sub>2</sub> and NbO<sub>x</sub>/CeO<sub>2</sub> catalysts in the ODHP reaction. Reaction conditions: 100 mg (60–80 mesh); C<sub>3</sub>H<sub>8</sub>/O<sub>2</sub>/Ar = 1.2:1.0:1.2; GHSV = 10000 mL h<sup>-1</sup> g<sup>-1</sup>.

Catalysts	S <sub>BET</sub> (m <sup>2</sup> /g)	C <sub>3</sub> H <sub>8</sub> Conversion (%)			C <sub>3</sub> H <sub>6</sub> Selectivity (%)		
		200 °C	250 °C	300 °C	200 °C	250 °C	300 °C
c-CeO <sub>2</sub>	34	0	0.5	3.2	0	2.4	2.8
0.5Nb/c-CeO <sub>2</sub>		3.5	4.1	8.1	0	0	11.9
1.1Nb/c-CeO <sub>2</sub>		3.7	4.4	7.3	0	0	15.3
2.8Nb/c-CeO <sub>2</sub>		1.9	2.1	3.7	0	4.3	29.5
6.8Nb/c-CeO <sub>2</sub>		2.2	2.6	3.2	0	1.7	27.9
8.7Nb/c-CeO <sub>2</sub>		0.3	0.6	0.7	0	6.1	31.2
r-CeO <sub>2</sub> -500	90	1.5	14.6	15.7	1.7	7.9	9.6
0.6Nb/r-CeO <sub>2</sub> -500		15.6	15.7	16.3	17.9	18.2	15.0
0.9Nb/r-CeO <sub>2</sub> -500		2.8	3.1	18.2	10.2	12.7	16.3
3.4Nb/r-CeO <sub>2</sub> -500		0.5	0.8	2.4	0	14.2	53.9
8.0Nb/r-CeO <sub>2</sub> -500		0.4	0.7	1.4	0	3.5	29.8
9.9Nb/r-CeO <sub>2</sub> -500		1.1	1.3	1.4	0	1.1	7.4
r-CeO <sub>2</sub> -700	46	0.9	16.0	16.4	0	1.0	10.6
0.5Nb/r-CeO <sub>2</sub> -700		1.2	2.1	18	0	0	13.3
1.0Nb/r-CeO <sub>2</sub> -700		1.5	1.8	16.6	0	0.2	17.8
1.9Nb/r-CeO <sub>2</sub> -700		2.9	3.4	3.6	0	3.2	30.6
5.1Nb/r-CeO <sub>2</sub> -700		3.2	3.5	3.9	0	0.6	8.2
10.2Nb/r-CeO <sub>2</sub> -700		3.4	3.6	3.9	0	0.4	3

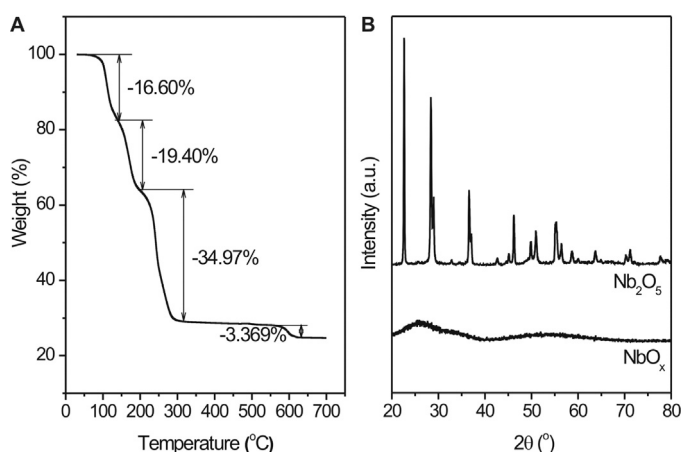


**Fig. 2.** (A) TGA profile of Nb(HC<sub>2</sub>O<sub>4</sub>)<sub>5</sub>·nH<sub>2</sub>O in air and (B) XRD patterns of commercial Nb<sub>2</sub>O<sub>5</sub> and NbO<sub>x</sub> acquired by calcining Nb(HC<sub>2</sub>O<sub>4</sub>)<sub>5</sub>·nH<sub>2</sub>O in air at 400 °C for 4 h.

r-CeO<sub>2</sub>-500 and r-CeO<sub>2</sub>-700 were measured to be 34, 90 and 46 m<sup>2</sup>/g. On basis of these data, we calculated the number of Nb atoms per nm<sup>2</sup> of CeO<sub>2</sub> surface for each NbO<sub>x</sub>/CeO<sub>2</sub> catalyst to denote the catalyst (Table 1). For an example, 0.5Nb/c-CeO<sub>2</sub> denotes the c-CeO<sub>2</sub>-supported NbO<sub>x</sub> catalyst with 0.5 Nb atom per nm<sup>2</sup> of c-CeO<sub>2</sub> surface. The largest Nb loadings of NbO<sub>x</sub>/CeO<sub>2</sub> catalysts in the present study gave 8.7Nb/c-CeO<sub>2</sub>, 9.9Nb/r-CeO<sub>2</sub>-500 and 10.2Nb/r-CeO<sub>2</sub>-700. Fig. 3 shows XRD patterns of various CeO<sub>2</sub> and NbO<sub>x</sub>/CeO<sub>2</sub> catalysts. Only diffraction patterns arising from CeO<sub>2</sub> appear in all samples, suggesting the formation of either highly dispersive or amorphous Nb-contained species. Inferred from the full width at half maximum (FWHM) of the CeO<sub>2</sub> diffraction peaks, the crystallinity of CeO<sub>2</sub> nanocrystals follows the order of c-CeO<sub>2</sub> > r-CeO<sub>2</sub>-700 > r-CeO<sub>2</sub>-500 and the loadings of NbO<sub>x</sub> do not deteriorate the crystallinity of CeO<sub>2</sub> supports. TEM and HRTEM images of 8.7Nb/c-CeO<sub>2</sub>, 9.9Nb/r-CeO<sub>2</sub>-500 and 10.2Nb/r-CeO<sub>2</sub>-700 catalysts are shown in Fig. 1D–F. c-CeO<sub>2</sub> and r-CeO<sub>2</sub>-700 supports retain their original morphologies in corresponding Nb/CeO<sub>2</sub> catalysts whereas the morphology of r-CeO<sub>2</sub>-500 in 9.9Nb/r-CeO<sub>2</sub>-500 changes quite a lot from its original morphology (Fig. 1D1, E1 and F1). HRTEM images identify CeNbO<sub>4</sub> ad-particles on c-CeO<sub>2</sub> in 8.7Nb/c-CeO<sub>2</sub>, Nb<sub>2</sub>O<sub>5</sub> and CeNbO<sub>4</sub> ad-particles on r-CeO<sub>2</sub>-500 in 9.9Nb/r-CeO<sub>2</sub>-500, and CeNbO<sub>4</sub> ad-particles on r-CeO<sub>2</sub>-700 in 10.2Nb/r-CeO<sub>2</sub>-700

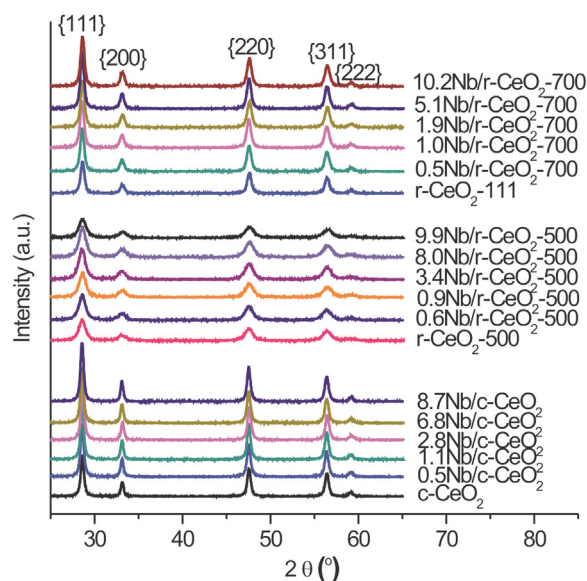


**Fig. 3.** XRD patterns of various CeO<sub>2</sub> and NbO<sub>x</sub>/CeO<sub>2</sub> catalysts.

(Fig. 1D2, E2 and F2); and some observed Nb<sub>2</sub>O<sub>5</sub> and CeNbO<sub>4</sub> in 9.9Nb/r-CeO<sub>2</sub>-500 and 10.2Nb/r-CeO<sub>2</sub>-700 catalysts adopt the morphologies of the r-CeO<sub>2</sub> supports. Besides Nb<sub>2</sub>O<sub>5</sub> and CeNbO<sub>4</sub> grains, amorphous adlayers thinner than 4 nm were observed to form on the CeO<sub>2</sub> surfaces in the NbO<sub>x</sub>/CeO<sub>2</sub> catalysts (Fig. 1D3, E3 and F3), and the c-CeO<sub>2</sub> (core)/amorphous adlayer (shell) structure could be observed in 8.7Nb/c-CeO<sub>2</sub>. The EDS analysis of the amorphous adlayer areas confirms the presence of Nb. These amorphous adlayers could be assigned to the amorphous NbO<sub>x</sub> formed by the decomposition of Nb(HC<sub>2</sub>O<sub>4</sub>)<sub>5</sub>·nH<sub>2</sub>O supported on CeO<sub>2</sub>. TEM and HRTEM observations demonstrated that the density of the amorphous NbO<sub>x</sub> adlayers is much higher than that of crystalline Nb<sub>2</sub>O<sub>5</sub> and CeNbO<sub>4</sub> in all NbO<sub>x</sub>/CeO<sub>2</sub> catalysts, agreeing with the XRD results.

Fig. 4 shows Nb 3d and Ce 4f XPS spectra of various catalysts. CeO<sub>2</sub> exhibits its Ce 4p<sub>3/2</sub> component at 206.6 eV that overlaps with the Nb 3d XPS feature [42]. The Nb 3d XPS spectra were fitted with XPSPEAK Version 4.1 software (Fig. 4A). The peak parameters of Ce 4p<sub>3/2</sub> component (peak position, FWHM and line-shape)



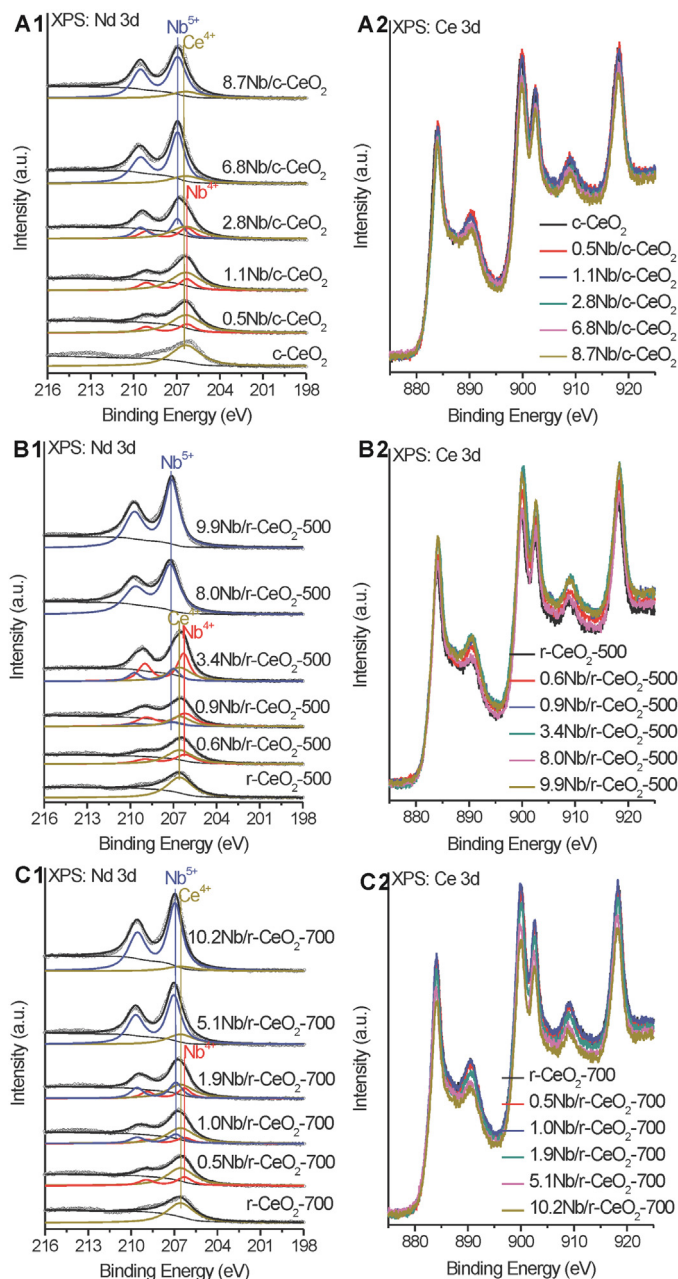


**Fig. 4.** Nb 3d and Ce 3d XPS spectra of (A) c-CeO<sub>2</sub> and NbO<sub>x</sub>/c-CeO<sub>2</sub>, (B) r-CeO<sub>2</sub>-500 and NbO<sub>x</sub>/r-CeO<sub>2</sub>-500 and (C) r-CeO<sub>2</sub>-700 and NbO<sub>x</sub>/r-CeO<sub>2</sub>-700 catalysts. In the Nb 3d XPS spectra, the scattered data, solid and thin lines respectively correspond to the experimental data, the peak-fitting data and the background.

were acquired from the bare CeO<sub>2</sub> supports and the peak parameters of the same Nb species (FWHM and line-shape) kept the same for all the spectra. Two Nb species with the Nb 3d<sub>5/2</sub> binding energy at 206.2 and 207.1 eV, respectively corresponding to Nb<sup>4+</sup> and Nb<sup>5+</sup> [43], were identified. Fig. 5 plots the percentage of Nb<sup>4+</sup> in Nb species (Nb<sup>4+</sup>/(Nb<sup>4+</sup> + Nb<sup>5+</sup>)) calculated from the integrating Nb<sup>4+</sup> and Nb<sup>5+</sup> XPS peak areas as a function of the Nb loading for the NbO<sub>x</sub>/c-CeO<sub>2</sub>, NbO<sub>x</sub>/r-CeO<sub>2</sub>-500 and NbO<sub>x</sub>/r-CeO<sub>2</sub>-700 catalysts. Only Nb<sup>4+</sup> exists at the lowest Nb loading in all NbO<sub>x</sub>/CeO<sub>2</sub> catalysts, and Nb<sup>5+</sup> generally grows at the expense of Nb<sup>4+</sup> with the increasing Nb loadings; however, the detailed evolution of formed Nb species varies with the CeO<sub>2</sub> support morphology. In the NbO<sub>x</sub>/c-CeO<sub>2</sub> catalysts, Nb<sup>4+</sup> still dominates in 1.1Nb/c-CeO<sub>2</sub>, and both Nb<sup>4+</sup> and Nb<sup>5+</sup> appear in 2.8Nb/c-CeO<sub>2</sub>, and

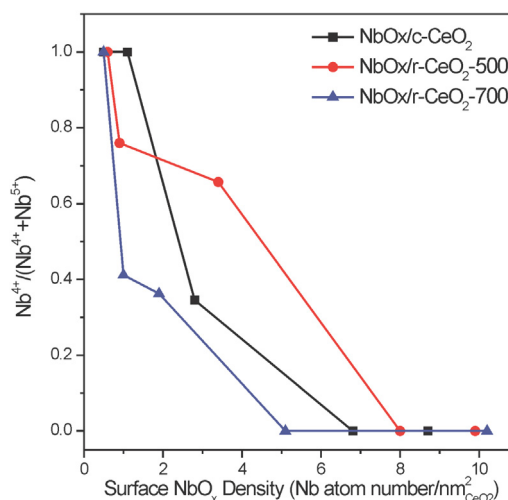


**Fig. 5.** The percentage of Nb<sup>4+</sup> in Nb species (Nb<sup>4+</sup>/(Nb<sup>4+</sup> + Nb<sup>5+</sup>)) calculated from the integrating Nb<sup>4+</sup> and Nb<sup>5+</sup> XPS peak areas as a function of the Nb loading for the NbO<sub>x</sub>/c-CeO<sub>2</sub>, NbO<sub>x</sub>/r-CeO<sub>2</sub>-500 and NbO<sub>x</sub>/r-CeO<sub>2</sub>-700 catalysts.

Nb<sup>5+</sup> dominates in 6.8Nb/c-CeO<sub>2</sub> and above. In the NbO<sub>x</sub>/r-CeO<sub>2</sub>-500 catalysts, both Nb<sup>4+</sup> and Nb<sup>5+</sup> appear in 0.9Nb/r-CeO<sub>2</sub>-500 and 3.4Nb/r-CeO<sub>2</sub>-500, and Nb<sup>5+</sup> dominates in 8.0Nb/r-CeO<sub>2</sub>-500 and above. In the NbO<sub>x</sub>/r-CeO<sub>2</sub>-700 catalysts, both Nb<sup>4+</sup> and Nb<sup>5+</sup> appear in 1.0Nb/r-CeO<sub>2</sub>-700 and 1.9Nb/r-CeO<sub>2</sub>-700, and Nb<sup>5+</sup> dominates in 5.1Nb/r-CeO<sub>2</sub>-700 and above. Meanwhile, the Nb<sup>5+</sup>/Nb<sup>4+</sup> ratio at similar Nb loadings follows the order of NbO<sub>x</sub>/r-CeO<sub>2</sub>-700 > NbO<sub>x</sub>/r-CeO<sub>2</sub>-500 > NbO<sub>x</sub>/c-CeO<sub>2</sub>. In the Nb(HC<sub>2</sub>O<sub>4</sub>)<sub>5</sub>·nH<sub>2</sub>O precursor Nb is Nb<sup>5+</sup>, thus Nb<sup>4+</sup> in the NbO<sub>x</sub>/CeO<sub>2</sub> catalysts should be formed by the redox reaction between Ce<sup>3+</sup> (oxygen vacancy) and Nb<sup>5+</sup> on the CeO<sub>2</sub> surface, and such a redox reaction is most facilitated on c-CeO<sub>2</sub> surface with the smallest BET specific surface area. The presence of Nb<sup>4+</sup> was previously observed in a Ce-Zr-Nb mixed oxides [43]. It is noteworthy that the VO<sub>x</sub> species supported on CeO<sub>2</sub> was reported always to be V<sup>5+</sup> [37–39]. These results suggest that the Nb-CeO<sub>2</sub> and V-CeO<sub>2</sub> interactions differ to some extent. The dispersion of the same supported species on CeO<sub>2</sub> usually varies with the CeO<sub>2</sub> BET specific surface area, but the formation of different supported species on CeO<sub>2</sub> can only be rated to the CeO<sub>2</sub> surface structure and reactivity. Therefore, CeO<sub>2</sub> nanocrystals exhibit the morphology-dependent surface reactivity toward the Ce<sup>3+</sup> (oxygen vacancy)/Nb<sup>5+</sup> redox reaction at low Nb loadings. With the Nb loading increasing, the formation of Nb<sup>5+</sup> becomes favorable, and Nb<sup>5+</sup> keeps growing at the expense of Nb<sup>4+</sup> and eventually dominates in all catalysts. Such processes also depend on the CeO<sub>2</sub> morphology, demonstrating the CeO<sub>2</sub> morphology-dependent Nb<sup>5+</sup>-CeO<sub>2</sub> interaction. No obvious changes associated with the Ce<sup>3+</sup> feature could be observed for the NbO<sub>x</sub>/CeO<sub>2</sub> catalysts with the same CeO<sub>2</sub> support but different Nb loadings (Fig. 4B). This is likely due to the fact that the Ce<sup>3+</sup> (oxygen vacancy)/Nb<sup>5+</sup> redox reaction only occurs at very low Nb loadings for all NbO<sub>x</sub>/CeO<sub>2</sub> catalysts.

The structures of various NbO<sub>x</sub>/CeO<sub>2</sub> catalysts were also studied with Raman spectroscopy (Fig. 6). CeO<sub>2</sub> exhibits a strong F<sub>2g</sub> vibrational peak at 464 cm<sup>-1</sup> and a weak oxygen vacancy defect-induced vibrational peak at 596 cm<sup>-1</sup> [37]. Both peaks were fitted and their integrating peak area ratio (I<sub>D</sub>/I<sub>F2g</sub>) was used to estimate the oxygen vacancy concentration. The I<sub>D</sub>/I<sub>F2g</sub> values of CeO<sub>2</sub> nanocrystals follow the order of r-CeO<sub>2</sub>-500 > c-CeO<sub>2</sub> > r-CeO<sub>2</sub>-700, thus the oxygen vacancy concentration is smaller in r-CeO<sub>2</sub>-700 than r-CeO<sub>2</sub>-500. The I<sub>D</sub>/I<sub>F2g</sub> values of CeO<sub>2</sub> in all Nb/CeO<sub>2</sub> catalysts do not change much from those of corresponding pure CeO<sub>2</sub> at low Nb loadings; however, they increase quickly with the Nb

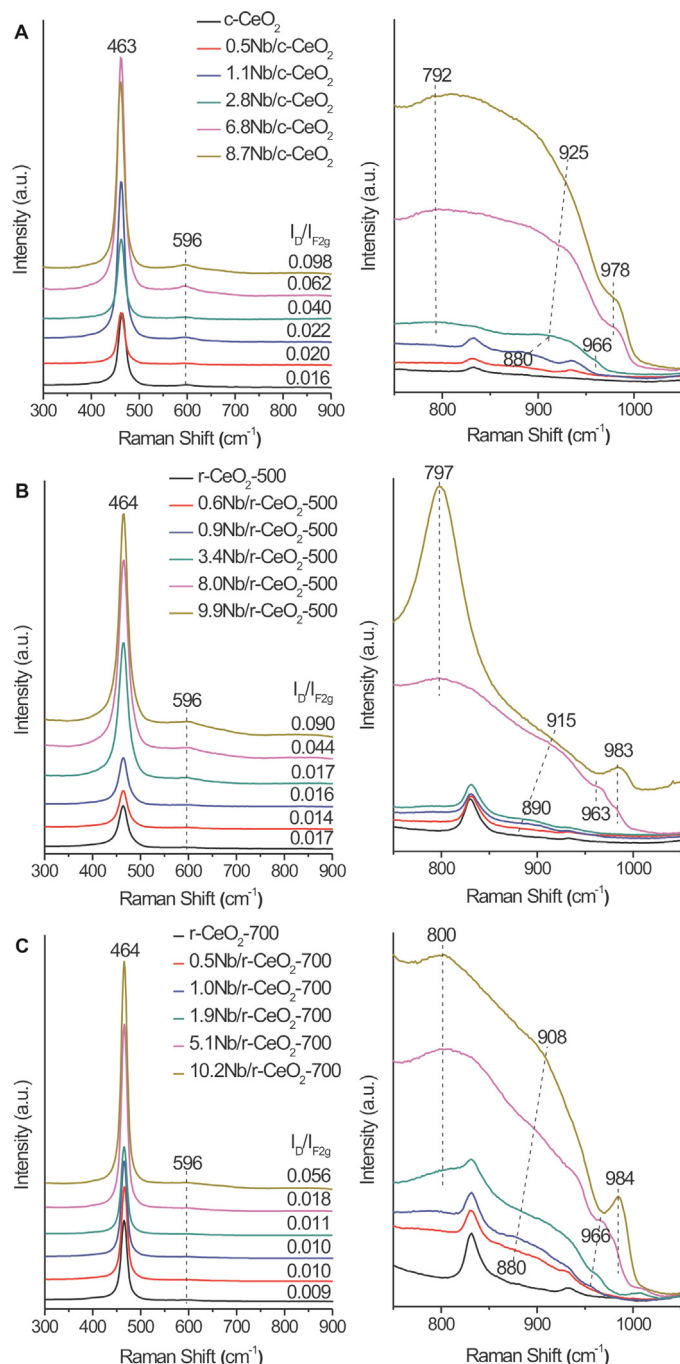


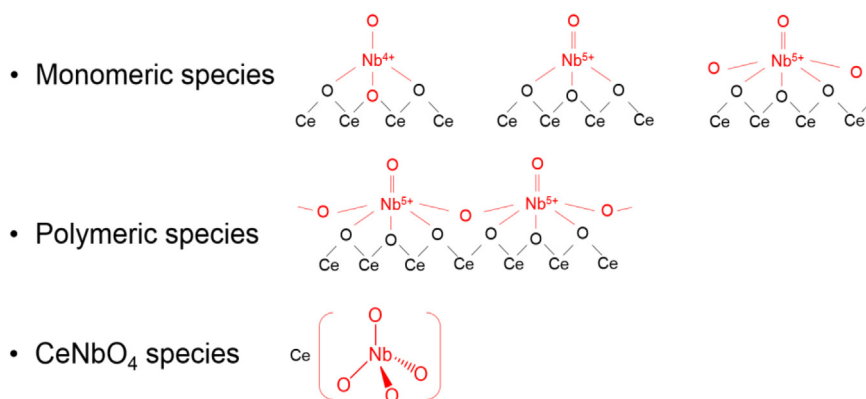
**Fig. 6.** Raman spectra of (A) c-CeO<sub>2</sub> and NbO<sub>x</sub>/c-CeO<sub>2</sub>, (B) r-CeO<sub>2</sub>-500 and NbO<sub>x</sub>/r-CeO<sub>2</sub>-500 and (C) r-CeO<sub>2</sub>-700 and NbO<sub>x</sub>/r-CeO<sub>2</sub>-700 catalysts.

loading at high Nb loadings and follow the order of NbO<sub>x</sub>/r-CeO<sub>2</sub>-500  $\cong$  NbO<sub>x</sub>/c-CeO<sub>2</sub> > NbO<sub>x</sub>/r-CeO<sub>2</sub>-700 at similar Nb loadings, the same as that of pure CeO<sub>2</sub> nanocrystals. Vibrational bands arising from various adsorbed oxygen species were also observed at 832 and 932 cm<sup>-1</sup> [44].

After the loading of NbO<sub>x</sub>, new vibrational bands at 984, 966, 880–925 and 800 cm<sup>-1</sup> appear in the Raman spectra and can be assigned respectively to the Nb=O stretch vibration of polymeric Nb species, the Nb=O stretch vibration of monomeric Nb species, the Nb–O stretch vibration of Nb species and the Nb–O stretch vibration of 4-coordinated CeNbO<sub>4</sub> [28,45–48]. With the increasing Nb loading in all NbO<sub>x</sub>/CeO<sub>2</sub> catalysts, only the 880–925 cm<sup>-1</sup> band appears initially and then the bands at 966, 984 and 800 cm<sup>-1</sup>

gradually develop. Thus we propose that the NbO<sub>x</sub> species in the NbO<sub>x</sub>/CeO<sub>2</sub> catalysts evolves from the monomeric Nb species only with the Nb–O stretch vibration (880 cm<sup>-1</sup>) to the monomeric Nb species with the Nb–O stretch vibration (908–925 cm<sup>-1</sup>) and Nb=O stretch vibration (966 cm<sup>-1</sup>), the polymeric Nb species with the Nb–O stretch vibration (908–925 cm<sup>-1</sup>) and Nb–O stretch vibration (980 cm<sup>-1</sup>) and the CeNbO<sub>4</sub> species with the Nb–O stretch vibration (800 cm<sup>-1</sup>) (Scheme 1). Indicated by the appearance of the 966 cm<sup>-1</sup> band, the formation of the monomeric Nb species only with the Nb–O stretch vibration follows the order of NbO<sub>x</sub>/r-CeO<sub>2</sub>-500 > NbO<sub>x</sub>/c-CeO<sub>2</sub> > NbO<sub>x</sub>/r-CeO<sub>2</sub>-700, which can be attributed to the largest specific surface area of r-CeO<sub>2</sub>-500. No monomeric V species only with the V–O stretch vibration was reported for VO<sub>x</sub>/CeO<sub>2</sub> samples [37–39]. Such a monomeric Nb species likely forms on the surface oxygen vacancy sites and the Nb<sup>5+</sup>/Ce<sup>3+</sup> redox reaction occurs within this Nb<sup>5+</sup>-O-Ce<sup>3+</sup> monomeric species to form the monomeric Nb<sup>4+</sup> species identified by XPS. And indicated by the XPS results, the formed monomeric Nb<sup>4+</sup> species should be most abundant on the c-CeO<sub>2</sub> support. CeNbO<sub>4</sub> in 9.9Nb/r-CeO<sub>2</sub>-500 exhibits a strong and sharp vibrational band, demonstrating its well crystallinity.

Fig. 7 shows H<sub>2</sub>-TPR profiles of various CeO<sub>2</sub> and NbO<sub>x</sub>/CeO<sub>2</sub> catalysts. CeO<sub>2</sub> nanocrystals exhibit a low-temperature surface reduction peak and a high-temperature subsurface reduction peak [49]. The initial H<sub>2</sub> reduction temperature follows the order of r-CeO<sub>2</sub>-500 < c-CeO<sub>2</sub> < r-CeO<sub>2</sub>-700 whereas the H<sub>2</sub> reduction peak follows r-CeO<sub>2</sub>-500 > c-CeO<sub>2</sub> > r-CeO<sub>2</sub>-700. This indicates that the reducibility of various CeO<sub>2</sub> nanocrystals follows r-CeO<sub>2</sub>-500 > c-CeO<sub>2</sub> > r-CeO<sub>2</sub>-700. The loading of NbO<sub>x</sub> affects the reduction behaviors of the CeO<sub>2</sub> support and the effect is strongly CeO<sub>2</sub> morphology-dependent. The reduction of Nb<sub>2</sub>O<sub>5</sub> was reported to occur above 800 °C [50] and could not be observed in our H<sub>2</sub>-TPR profiles. For the NbO<sub>x</sub>/c-CeO<sub>2</sub> catalysts, the low-temperature surface reduction peak of c-CeO<sub>2</sub> reduces with the Nb loadings up to 6.8Nb/nm<sup>2</sup> and slightly resumes at a Nb loading of 8.7 Nb/nm<sup>2</sup>. A new tiny reduction peak emerges at 550 °C in 6.8Nb/c-CeO<sub>2</sub> and grows into a sharp peak at 540 °C. This feature can be assigned to the reduction of CeNbO<sub>4</sub> formed on c-CeO<sub>2</sub> at high Nb loadings and its fast reduction kinetics indicates the occurrence of the reductive decomposition of CeNbO<sub>4</sub>. The H<sub>2</sub>-TPR results demonstrate that the NbO<sub>x</sub>-c-CeO<sub>2</sub> interactions stabilize the surface lattice oxygen of c-CeO<sub>2</sub> and suppress the surface reduction whereas the transformation of dispersive NbO<sub>x</sub> into CeNbO<sub>4</sub> at high Nb loadings alleviates the stabilization effect. Similar H<sub>2</sub>-TPR results were also observed for the NbO<sub>x</sub>/r-CeO<sub>2</sub>-500 catalysts. The low-temperature surface reduction peak of r-CeO<sub>2</sub>-500 reduces with the Nb loadings up to 8.0 Nb/nm<sup>2</sup> and the initial H<sub>2</sub> reduction temperatures for the 3.4Nb/r-CeO<sub>2</sub>-500 and 8.0Nb/r-CeO<sub>2</sub>-500 catalysts are about 50 °C higher than that of r-CeO<sub>2</sub>-500. A sharp and strong reduction peak corresponding to the reductive decomposition of CeNbO<sub>4</sub> appears at 590 °C for the 8.0Nb/r-CeO<sub>2</sub>-500 catalyst. These demonstrate both the stabilization of the surface lattice oxygen of r-CeO<sub>2</sub>-500 by the NbO<sub>x</sub>-r-CeO<sub>2</sub>-500 interactions and the high dispersion of NbO<sub>x</sub> species and NbCeO<sub>4</sub> on r-CeO<sub>2</sub>-500. With the increase of the Nb loading from 8.7 Nb/nm<sup>2</sup> to 9.9 Nb/nm<sup>2</sup>, the NbCeO<sub>4</sub> reduction peak slightly weakens and shifts down to 580 °C; meanwhile, the low-temperature surface reduction peak of r-CeO<sub>2</sub>-500 resumes quite a lot. These indicate the transformation of highly dispersive CeNbO<sub>4</sub> in 8.8Nb/r-CeO<sub>2</sub>-500 into CeNbO<sub>4</sub> aggregates in 9.9Nb/r-CeO<sub>2</sub>-500, in consistence with previous Raman results that NbCeO<sub>4</sub> in 9.9Nb/r-CeO<sub>2</sub>-500 is well crystallized. The effect of NbO<sub>x</sub> on the reducibility of r-CeO<sub>2</sub>-700 is in contrast to those on c-CeO<sub>2</sub> and r-CeO<sub>2</sub>-500. The low-temperature surface reduction peak of r-CeO<sub>2</sub>-700 increases and its initial reduction temperature shifts to lower temperatures with the Nb loading increasing up to 5.1Nb/nm<sup>2</sup>. A small and sharp reduction peak corresponding to the reductive decomposition of



**Scheme 1.** Proposed  $\text{NbO}_x$  species on  $\text{CeO}_2$ . “O” and “O” represent oxygen atoms in  $\text{CeO}_2$  and  $\text{NbO}_x$ , respectively.

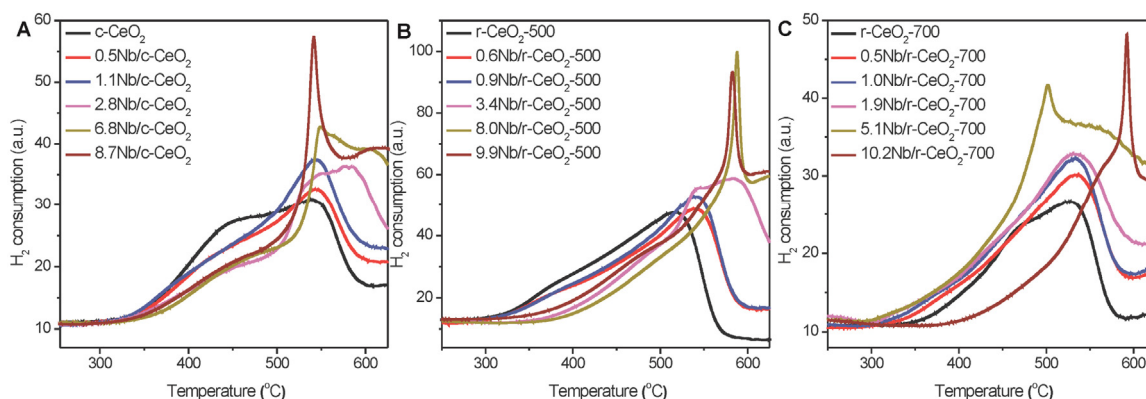


**Fig. 7.**  $\text{H}_2$ -TPR profiles of (A) c- $\text{CeO}_2$  and  $\text{NbO}_x/\text{c-CeO}_2$ , (B) r- $\text{CeO}_2$ -500 and  $\text{NbO}_x/\text{r-CeO}_2$ -500 and (C) r- $\text{CeO}_2$ -700 and  $\text{NbO}_x/\text{r-CeO}_2$ -700 catalysts.

$\text{CeNbO}_4$  appears at  $500^\circ\text{C}$  for the 5.1Nb/r- $\text{CeO}_2$ -500 catalyst. These demonstrate that the  $\text{NbO}_x$ -r- $\text{CeO}_2$ -700 interactions destabilize the surface lattice oxygen of r- $\text{CeO}_2$ -700 and promote the surface reduction. With the increase of the Nb loading from 5.1 Nb/nm<sup>2</sup> to 10.2 Nb/nm<sup>2</sup>, the  $\text{NbCeO}_4$  reduction peak greatly increases and shifts upward to  $590^\circ\text{C}$ ; meanwhile, the low-temperature surface reduction peak of r- $\text{CeO}_2$ -700 is strongly suppressed. These suggest the formation of highly dispersive  $\text{NbCeO}_4$  on r- $\text{CeO}_2$ -700 in 10.2Nb/r- $\text{CeO}_2$ -700. The  $\text{CeNbO}_4$  reduction peaks of 8.7Nb/c- $\text{CeO}_2$ , 9.9Nb/r- $\text{CeO}_2$ -500 and 10.2Nb/CeO<sub>2</sub>-700 imply that the dispersion and stability of  $\text{CeNbO}_4$  should follow an order of 10.2Nb/CeO<sub>2</sub>-700  $\cong$  9.9Nb/r- $\text{CeO}_2$ -500 > 8.7Nb/c- $\text{CeO}_2$ .

Above observed morphology-dependent  $\text{NbO}_x$ - $\text{CeO}_2$  interactions of c- $\text{CeO}_2$ , r- $\text{CeO}_2$ -500 and r- $\text{CeO}_2$ -700 could be related to their exposed crystal planes. c- $\text{CeO}_2$  is enclosed with six {100} facets. Our argument that r- $\text{CeO}_2$ -500 exposes mainly  $\text{CeO}_2$  {110} and {100} facets while r- $\text{CeO}_2$ -700 exposes mainly  $\text{CeO}_2$  {111} and {110} facets is supported by the smaller oxygen vacancy concentration of r- $\text{CeO}_2$ -700 than r- $\text{CeO}_2$ -500 and the poorer reducibility of r- $\text{CeO}_2$ -700 than r- $\text{CeO}_2$ -500. Theoretical calculation studies show that the oxygen vacancy formation energy on different  $\text{CeO}_2$  crystal planes  $\text{CeO}_2$  follows the order of (110) < (100) < (111) [51,52] and the stability of the  $\text{CeO}_2$  (111), (100) and (110) surfaces follows the order of (111) > (110) > (100) [51,53]. Due to the less oxygen vacancies/ $\text{Ce}^{3+}$  on  $\text{CeO}_2$  {111} than  $\text{CeO}_2$  {110} and {100}, the  $\text{Nb}^{4+}$  species formed by the  $\text{Nb}^{5+}/\text{Ce}^{3+}$  redox reaction is smallest on r- $\text{CeO}_2$ -700. The interactions of monomeric and polymeric  $\text{NbO}_x$  species with  $\text{CeO}_2$  surfaces involve the surface lattice oxygen of  $\text{CeO}_2$ , and stabilize the surface lattice oxygen of  $\text{CeO}_2$  {110} and {100} facets but destabilize the surface lattice oxygen of  $\text{CeO}_2$  {111} facet. Meanwhile,  $\text{NbO}_x$  reacts with  $\text{CeO}_2$  at large Nb loadings and

the formed  $\text{CeNbO}_4$  is more stable on  $\text{CeO}_2$  {110} and {111} facets than on  $\text{CeO}_2$  {100} facet.

Various  $\text{CeO}_2$  and  $\text{NbO}_x/\text{CeO}_2$  samples were examined as the catalysts for the ODHP reaction up to  $300^\circ\text{C}$ . The catalytic performances turn out not to be good, and the  $\text{C}_3\text{H}_8$  conversions and  $\text{C}_3\text{H}_6$  selectivities are summarized in Table 1. The  $\text{C}_3\text{H}_8$  conversions below 10% increase with the reaction temperature whereas those above 10% do not. This indicates that the heat exerted by the exothermic ODHP reaction at  $\text{C}_3\text{H}_8$  conversions larger than 10% should be strong enough to affect the temperature of catalyst bed under the employed ODHP reaction condition. CO,  $\text{CO}_2$  and  $\text{C}_3\text{H}_6$  are the main products of the ODHP reaction, and other minor products are  $\text{CH}_4$  and  $\text{C}_2\text{H}_4$ . The calculated carbon balances are always higher than 97%. Taking the catalytic performance of 0.6Nb/r- $\text{CeO}_2$ -500 at  $200^\circ\text{C}$  as example, the conversions of  $\text{C}_3\text{H}_6$  and  $\text{O}_2$  are 15.6% and 100%, respectively; and the selectivities of CO,  $\text{CO}_2$ ,  $\text{C}_3\text{H}_6$ ,  $\text{C}_2\text{H}_4$  and CH are 71.0%, 7.7%, 17.9%, 0.6% and 0.2%, respectively.

Although with poor catalytic performances, the  $\text{CeO}_2$  and  $\text{NbO}_x/\text{CeO}_2$  catalysts exhibit obvious  $\text{CeO}_2$  morphology-dependent  $\text{C}_3\text{H}_8$  conversions and  $\text{C}_3\text{H}_6$  selectivities. R- $\text{CeO}_2$ -500 and r- $\text{CeO}_2$ -700 exhibit similar  $\text{C}_3\text{H}_8$  conversion and  $\text{C}_3\text{H}_6$  selectivity whereas c- $\text{CeO}_2$  shows negligible catalytic activity. These imply that  $\text{CeO}_2$  {110} facets present on both r- $\text{CeO}_2$ -500 and r- $\text{CeO}_2$ -700 should be the active  $\text{CeO}_2$  facet to catalyze the ODHP reaction. This could be related with the DFT calculation results that the  $\text{CeO}_2$  {110} facet with the smallest oxygen vacancy formation energy is more catalytic active than  $\text{CeO}_2$  {111} and {110} facets with larger oxygen vacancy formation energies [51,52], implying that the ODHP reaction catalyzed by  $\text{CeO}_2$  at low temperatures should follow the Mars van Krevelen mechanism. The  $\text{C}_3\text{H}_8$  conversion of Nb/c- $\text{CeO}_2$  slightly increases with the Nb loading up to the Nb loading of



1.1Nb/nm<sup>2</sup> and then decreases. A loading of 0.6 Nb/nm<sup>2</sup> enhances the C<sub>3</sub>H<sub>8</sub> conversion of r-CeO<sub>2</sub>-500 at 200 °C quite much, but the further increase of the Nb loading results in the decrease of the C<sub>3</sub>H<sub>8</sub> conversion. The loading of NbO<sub>x</sub> decreases the catalytic activity of r-CeO<sub>2</sub>-700. Comparing the NbO<sub>x</sub> species and catalytic activity of various NbO<sub>x</sub>/CeO<sub>2</sub> catalysts, the highly dispersive monomeric Nb<sup>4+</sup> species promotes the catalytic activity of CeO<sub>2</sub> but other NbO<sub>x</sub> species poison the catalytic activity of CeO<sub>2</sub>. As shown in Scheme 1, the formation of highly dispersive monomeric Nb<sup>4+</sup> species is accompanied by the refilling of surface oxygen vacancies in CeO<sub>2</sub> and likely enhances the activity of neighboring surface lattice oxygen in CeO<sub>2</sub> for the ODHP reaction whereas the formation of other NbO<sub>x</sub> species likely decreases the available surface lattice oxygen in CeO<sub>2</sub> for the ODHP reaction. Although CeO<sub>2</sub> and NbO<sub>x</sub>/CeO<sub>2</sub> are poor in catalyzing the ODHP reaction, the present results add a solid example to vindicate the morphology engineering strategy to modify the structure and catalytic performance of CeO<sub>2</sub>-based catalysts; moreover, the 0.6Nb/r-CeO<sub>2</sub>-500 catalyst shows some promise as a candidate for the low-temperature ODHP reaction. Future works will focus on the fabrication of the 0.6Nb/r-CeO<sub>2</sub>-500-based low-temperature ODHP catalysts.

#### 4. Conclusions

NbO<sub>x</sub>/CeO<sub>2</sub> catalysts employing c-CeO<sub>2</sub>, r-CeO<sub>2</sub>-500 and r-CeO<sub>2</sub>-700 as the supports exhibit CeO<sub>2</sub> morphology-dependent NbO<sub>x</sub>-CeO<sub>2</sub> interaction, structures and catalytic performances in the oxidative dehydrogenation of propane reaction. The supported NbO<sub>x</sub> species evolve with the increasing Nb loading from the monomeric Nb species to the polymeric Nb species and the CeNbO<sub>4</sub> species. The monomeric Nb<sup>5+</sup> species interacting with oxygen vacancy/Ce<sup>3+</sup> on CeO<sub>2</sub> can be reduced to form the monomeric Nb<sup>4+</sup> species. The formed monomeric Nb species is most abundant on the r-CeO<sub>2</sub>-500 support while the formed monomeric Nb<sup>4+</sup> species is most abundant on the c-CeO<sub>2</sub> support. The loading of NbO<sub>x</sub> suppresses the surface reduction of c-CeO<sub>2</sub> and r-CeO<sub>2</sub>-500 but promotes the surface reduction of r-CeO<sub>2</sub>-700. A NbO<sub>x</sub>/r-CeO<sub>2</sub>-500 catalyst with the Nb loading of 0.6 Nb/nm<sup>2</sup> shows some promise as a candidate for the low-temperature ODHP reaction. These results add a solid example to vindicate the morphology engineering strategy to modify the structure and catalytic performance of CeO<sub>2</sub>-based catalysts and understand the fundamental CeO<sub>2</sub>-involved catalysis.

#### Acknowledgements

This work was financially supported by National Basic Research Program of China (2013CB933104), National Natural Science Foundation of China (21525313, 21173204, U1332113), Chinese Academy of Sciences (KJZD-EW-M03), MOE Fundamental Research Funds for the Central Universities (WK2060030017), and Collaborative Innovation Center of Suzhou Nano Science and Technology.

#### References

- [1] H.H. Kung, *Adv. Catal.* 40 (1994) 1–35.
- [2] A. Held, J. Kowalska, K. Nowińska, *Appl. Catal. B: Environ.* 64 (2006) 201–208.
- [3] F.M. Bautista, J.M. Campelo, D. Luna, J.M. Marinas, R.A. Quirós, A.A. Romero, *Appl. Catal. B: Environ.* 70 (2007) 611–620.
- [4] K.N. Rao, B.M. Reddy, B. Abhishek, Yeong-Hui Seo, Nanzhe Jiang, S.-E. Park, *Appl. Catal. B: Environ.* 91 (2009) 649–656.
- [5] B. Frank, A. Dinse, O. Ovsitser, E.V. Kondratenko, R. Schomäcker, *Appl. Catal. A: Gen.* 323 (2007) 66–76.
- [6] V.C. Corberán, *Catal. Today* 99 (2005) 33–41.
- [7] F. Cavani, F. Trifiro, *Catal. Today* 24 (1995) 307–313.
- [8] F. Cavani, N. Ballarini, A. Cericola, *Catal. Today* 127 (2007) 113–131.
- [9] T. Blasco, J.L. Nieto, *Appl. Catal. A: Gen.* 157 (1997) 117–142.
- [10] E. Mamedov, V.C. Corberán, *Appl. Catal. A: Gen.* 127 (1995) 1–40.
- [11] R. Grabowski, *Catal. Rev.* 48 (2006) 199–268.
- [12] P. Boizumault-Moriceau, A. Pennequin, B. Grzybowska, Y. Barbaux, *Appl. Catal. A: Gen.* 245 (2003) 55–67.
- [13] L. Jałowicki-Duhamel, A. Ponchel, C. Lamonier, A. D'Huysser, Y. Barbaux, *Langmuir* 17 (2001) 1511–1517.
- [14] W.-S. Dong, H.-S. Roh, K.-W. Jun, S.-E. Park, Y.-S. Oh, *Appl. Catal. A: Gen.* 226 (2002) 63–72.
- [15] W. Daniell, A. Ponchel, S. Kuba, F. Anderle, T. Weingand, D. Gregory, H. Knözinger, *Top. Catal.* 20 (2002) 65–74.
- [16] C.A. Chagas, L.C. Dieguez, M. Schmal, *Catal. Lett.* 142 (2012) 753–762.
- [17] M.N. Taylor, A.F. Carley, T.E. Davies, S.H. Taylor, *Top. Catal.* 52 (2009) 1660–1668.
- [18] K. Tanabe, S. Okazaki, *Appl. Catal. A: Gen.* 133 (1995) 191–218.
- [19] K. Tanabe, *Catal. Today* 78 (2003) 65–77.
- [20] R. Burch, R. Swarnakar, *Appl. Catal.* 70 (1991) 129–148.
- [21] E. Heracleous, A. Lemonidou, *J. Catal.* 237 (2006) 162–174.
- [22] E. Heracleous, A. Lemonidou, *J. Catal.* 237 (2006) 175–189.
- [23] J. Millet, H. Roussel, A. Pigamo, J. Dubois, J. Jumas, *Appl. Catal. A: Gen.* 232 (2002) 77–92.
- [24] Q. Xie, L. Chen, W. Weng, H. Wan, *J. Mol. Catal. A: Chem.* 240 (2005) 191–196.
- [25] P. Botella, E. García-González, A. Dejoz, J.L. Nieto, M. Vázquez, J. González-Calbet, *J. Catal.* 225 (2004) 428–438.
- [26] D. Stošić, S. Bennici, V. Rakić, A. Auroux, *Catal. Today* 192 (2012) 160–168.
- [27] E.d.O. Jardim, S. Rico-Francés, F. Coloma, J.A. Anderson, E.V. Ramos-Fernandez, J. Silvestre-Albero, A. Sepúlveda-Escribano, *Appl. Catal. A: Gen.* 492 (2015) 201–211.
- [28] R. Qu, X. Gao, K. Cen, J. Li, *Appl. Catal. B: Environ.* 142 (2013) 290–297.
- [29] M. Casapu, A. Bernhard, D. Peitz, M. Mehning, M. Elsener, O. Kröcher, *Appl. Catal. B: Environ.* 103 (2011) 79–84.
- [30] K. Yashiro, T. Suzuki, A. Kaimai, H. Matsumoto, Y. Nigara, T. Kawada, J. Mizusaki, J. Sfeir, *Solid State Ionics* 175 (2004) 341–344.
- [31] J. Li, C. Wang, C. Huang, W. Weng, H. Wan, *Catal. Lett.* 137 (2010) 81–87.
- [32] H.-X. Mai, L.-D. Sun, Y.-W. Zhang, R. Si, W. Feng, H.-P. Zhang, H.-C. Liu, C.-H. Yan, *J. Phys. Chem. B* 109 (2005) 24380–24385.
- [33] Y. Gao, W. Wang, S. Chang, W. Huang, *ChemCatChem* 5 (2013) 3610–3620.
- [34] W. Huang, Y. Gao, *Catal. Sci. Technol.* 4 (2014) 3772–3784.
- [35] S. Chang, M. Li, Q. Hua, L. Zhang, Y. Ma, B. Ye, W. Huang, *J. Catal.* 293 (2012) 195–204.
- [36] Y. Gao, R. Li, S. Chen, L. Luo, T. Cao, W. Huang, *Phys. Chem. Chem. Phys.* 17 (2015) 31862–31871.
- [37] Z. Wu, V. Schwartz, M. Li, A.J. Rondinone, S.H. Overbury, *J. Phys. Chem. Lett.* 3 (2012) 1517–1522.
- [38] Z. Wu, M. Li, S.H. Overbury, *ChemCatChem* 4 (2012) 1653–1661.
- [39] Z. Wu, A.J. Rondinone, I.N. Ivanov, S.H. Overbury, *J. Phys. Chem. C* 115 (2011) 25368–25378.
- [40] N. Ta, J. Liu, S. Chenna, P.A. Crozier, Y. Li, A. Chen, W. Shen, *J. Am. Chem. Soc.* 134 (2012) 20585–20588.
- [41] Z.A. Qiao, Z. Wu, S. Dai, *ChemSusChem* 6 (2013) 1821–1833.
- [42] E. Paparazzo, G. Ingo, N. Zaccchetti, *J. Vac. Sci. Technol. A* 9 (1991) 1416–1420.
- [43] H. Ardelean, I. Frateur, P. Marcus, *Corros. Sci.* 50 (2008) 1907–1918.
- [44] I.E. Wachs, C.A. Roberts, *Chem. Soc. Rev.* 39 (2010) 5002–5017.
- [45] L.J. Burcham, J. Datka, I.E. Wachs, *J. Phys. Chem. B* 103 (1999) 6015–6024.
- [46] C. García-Sancho, J. Cecilia, A. Moreno-Ruiz, J. Mérida-Robles, J. Santamaría-González, R. Moreno-Tost, P. Maireles-Torres, *Appl. Catal. B: Environ.* 179 (2015) 139–149.
- [47] J.M. Jehng, I.E. Wachs, *Chem. Mater.* 3 (1991) 100–107.
- [48] I.E. Wachs, *Catal. Today* 27 (1996) 437–455.
- [49] Z. Wu, M. Li, S.H. Overbury, *J. Catal.* 285 (2012) 61–73.
- [50] I.E. Wachs, Y. Chen, J.-M. Jehng, L.E. Briand, T. Tanaka, *Catal. Today* 78 (2003) 13–24.
- [51] M. Nolan, S.C. Parker, G.W. Watson, *Surf. Sci.* 595 (2005) 223–232.
- [52] M. Huang, S. Fabris, *J. Phys. Chem. C* 112 (2008) 8643–8648.
- [53] T. Sayle, S. Parker, C. Catlow, *Surf. Sci.* 316 (1994) 329–336.